JOURNAL OF PROPULSION AND POWER
Vol. 19, No. 6, November–December 2003

Three-Dimensional Particle Simulations of Ion-Optics Plasma Flow and Grid Erosion

Joseph Wang*
Virginia Polytechnic Institute and State University, Blacksburg, Virginia 24061-0203
and
James Polk,† John Brophy,‡ and Ira Katz§
Jet Propulsion Laboratory, California Institute of Technology, Pasadena, California 91109

A fully three-dimensional computer particle simulation model for ion optics is developed. This model allows multiple apertures to be included explicitly in the simulation domain and determines the upstream sheath and downstream beam neutralization through simulations. Simulations are performed for the NSTAR ion-thruster optics, and results are compared with grid-erosion measurements obtained during NSTAR long-duration test. It is shown that the simulation not only predicts accurately all of the features in the measured erosion pattern but also gives excellent quantitative agreement with the measured erosion depth.

Nomenclature

$\boldsymbol{E}$	=	electric field
n_b, n_n, n_{cex}	=	number density for the beam ions, the neutrals, and the charge-exchange ions, respectively
n_0,n_∞	=	discharge plasma and downstream plasma density, respectively
R	=	depth erosion rate
T_{e0}, $T_{e\infty}$	=	electron temperature in the upstream and the downstream plasma, respectively
T_w	=	discharge chamber wall temperature
Y	=	sputter yield
λ_{D0}	=	Debye length in the discharge plasma
σ_{cex}	=	charge-exchange collision cross section
Φ	=	electric potential
Φ_0, Φ_∞	=	upstream and downstream plasma potential, respectively

I. Introduction

ION propulsion is a critical enabling technology for future deep-space missions. A key issue in ion-thruster development is grid design and thruster service life, which is primarily limited by grid erosion. In recent years ion-optics modeling has become an ever more important tool to help improve grid design, predict thruster service life, and understand thruster failure modes.

The nature of plasma flow in ion optics has rendered computer particle simulation, which solves plasma particle trajectory, space charge, and the Poisson's equation self-consistently, as the preferred modeling method. Some recent ion-optics simulation studies can be found in Refs. 1–8 and references therein. The majority of ion-optics models are axisymmetric models. The axisymmetric formulation does not take into account the hexagonal layout of the ion-optics aperture array. The currently available three-dimensional ion-optics models are all designed for a single grid aperture by considering the six-fold hexagonal symmetry of the aperture array, and simulations are performed for a cross section of $\frac{1}{12}$ of a single aperture (30×60 deg right-triangle cross section). Because of computational constraints, almost all published studies limit the simulation domain to a relatively small region surrounding the optics. Some models use a predetermined beam ion emission surface to represent the effects of the upstream presheath. No simulations have explicitly included the region far downstream of the optics and identified the location where charge-exchange ions start to backflow. Obviously, a simulation setup that fails to account for all impingement ions from the downstream region will result in an underprediction of the accel grid current.

In this paper we present a more generalized, fully three-dimensional ion-optics model. The code is designed in such a way that not only single aperture but also multiple apertures can be included explicitly in the simulation domain. In addition, no assumptions are made to simplify the upstream and downstream boundary conditions. The upstream sheath and ion beam extraction from the discharge plasma are determined self-consistently in the simulation. The simulation is extended into the region far downstream of the accelerator grid. The location where beamlets become neutralized and charge-exchange ions start to backflow is resolved. The results will show that both the three-dimensional beamlet structure and the far-downstream region have a significant effect on grid erosion.

This code is applied to model ion-optics plasma flow for the NSTAR ion thruster. During the long-duration test (LDT) of the Deep Space 1 flight spare NSTAR thruster performed at Jet Propulsion Laboratory, both laser profilometer measurements and posttest destructive examinations were performed to obtain the grid-erosion pattern and erosion depth.[9] In this paper we also compare grid erosion obtained from simulation results and that from erosion measurements during LDT. The results will show that this new model not only predicts accurately all features in the measured erosion pattern but also gives excellent quantitative agreement with measured erosion depth.

Section II discusses the simulation model. Section III presents typical simulation results. Section IV compares simulation results with NSTAR LDT grid-erosion measurements. Section V contains a summary and conclusions.

II. Simulation Model

The simulation model includes a set of three particle-in-cell (PIC) codes: an ion beamlet code, a neutral particle code, and a charge-exchange ion code. In this model propellant ions, charge-exchange ions, and neutrals are treated as macroparticles. The ion beamlet code is used to simulate ion beam extraction from the discharge plasma. As the space charge carried by charge-exchange ions is negligible compared to that of beam ions, the charge-exchange ions

Received 5 June 2002; revision received 6 December 2002; accepted for publication 24 January 2003.

*Associate Professor; jowang@vt.edu. Associate Fellow AIAA.
†Principal Engineer, MS 125-109. Member AIAA.
‡Principal Engineer, MS 125-109. Member AIAA.
§Group Supervisor, MS 125-109. Member AIAA.

have little effects on the beam ion trajectories and are thus not included in the ion beamlet simulation. The neutral particle code is used to track the flow of unionized propellant particles. We consider that the unionized propellant particles exit through the grids in free molecular flow with a temperature close to the thruster discharge chamber wall temperature ($T_w \sim 500$ K). When neutral particles hit the optics walls, they undergo a diffusive reflection. Once a steady state has been achieved for beam ions and neutral particles, the beam ions and neutrals are frozen, and we start charge-exchange ion simulation. Charge-exchange ions are generated according to the volumetric charge-exchange ion production rate calculated from ion beamlet and neutral density profiles.

The major challenge in applying the particle simulation method as a design tool is to build up a code that is sophisticated enough so the complex geometry associated with the optics can be modeled properly and yet computationally efficient enough so that large-scale three-dimensional particle simulations can be performed routinely within a reasonable time period. Complex geometries are usually best handled by tetrahedral cells or unstructured grids and a finite element based formulation. However, a tetrahedral-cell-based or unstructured-grid-based particle code can be significantly computationally more expensive than a standard orthogonal grid PIC code. In a standard orthogonal grid PIC code the location of the memory of quantities defined in neighboring cells can be found trivially via indexing. This is in contrast to an unstructured grid code where the neighbors of a given cell must be found by lookups in a table or other methods requiring additional memory references. Moreover, for either a tetrahedral-cell-based or unstructured-grid-based PIC code a fairly complex scheme is typically needed to determine a particle's new cell.[10] These added complexities can make large-scale three-dimensional ion-optics simulations prohibitively expensive because a particle code spends a great deal of its computing time pushing particles and performing particle-grid interpolations.[11] Out of consideration for computational efficiency for large-scale simulations, we choose to use orthogonal grids and solve the electric field using a finite-difference formulation. To resolve the geometry associated with optics apertures, a method of subgrid-scale placement of boundaries[12] is used. This method explicitly includes the location of the optics wall in relation to the computational mesh so that the placement of the object boundary is not restricted to the mesh points. We find that such an approach is sufficient for this problem and allows us to retain the computational efficiency associated with an orthogonal grid PIC code.

The simulation domain can be set up to include multiple apertures (Fig. 1). To perform local simulations surrounding a few beamlets, one takes advantage of the boundary conditions presented by symmetric surfaces. The "minimum" simulation domain would be a domain with a cross section including two quarter-size holes (Fig. 2). Note that this minimum cross section fully accounts for the three-dimensional geometric effects from a hexagonal layout of the aperture arrays. The simulation domain shown in Fig. 2 will be used in simulations presented in this paper.

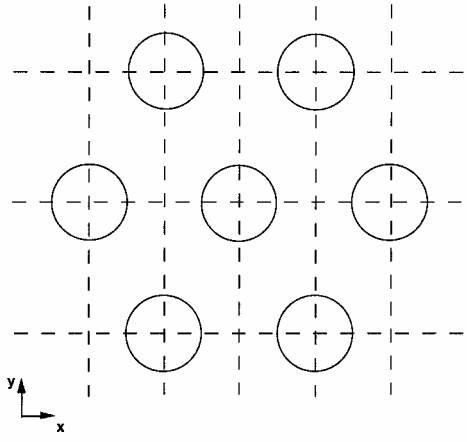

Fig. 1 Cross section of a simulation domain with multiple apertures.

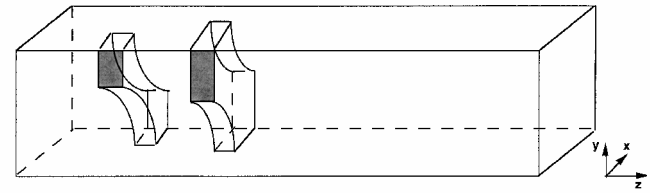

Fig. 2 Simulation domain with two quarter-size apertures.

Along the acceleration direction (z direction) the upstream boundary represents the discharge plasma, which has a plasma potential Φ_0, density n_0, and electron temperature T_{e0}. We make no assumptions on the plasma sheath upstream of the screen grid. The upstream boundary is placed far upstream from the screen grid. The ion current is extracted, and the plasma sheath is determined self-consistently in the simulation. The downstream boundary represents the neutralized propellant plasma, which has a plasma potential Φ_∞, density n_∞, and electron temperature $T_{e\infty}$. We make no assumptions on beamlet neutralization location. The downstream boundary is placed far downstream from the accel grid so that the beamlet neutralization location is explicitly included in the simulation domain. As the downstream boundary represents a neutralized plasma, we take the downstream plasma density n_∞ to be the average ion density near the downstream boundary and update n_∞ at every time step in the simulation.

The electric field, space charge, and ion trajectories are solved self-consistently from Poisson's equation

$$\nabla^2\Phi = -4\pi[n_i - n_e] \tag{1}$$

and Newtown's second law applied to macroparticles representing ions

$$\frac{\mathrm{d}m\boldsymbol{V}}{\mathrm{d}t} = q\boldsymbol{E}, \qquad \frac{\mathrm{d}\boldsymbol{x}}{\mathrm{d}t} = \boldsymbol{V} \tag{2}$$

Similar to the approach used in other ion-optics codes, the electrons are assumed to be an isothermal fluid. A Boltzmann relationship between the electron density n_e and local electrostatic potential Φ is used in regions upstream of the screen grid and downstream of the acceleration grid: Specifically, the electron density in the region upstream of the screen grid is given by

$$n_e = n_0 \exp[(\Phi - \Phi_0)/T_{e0}], \qquad \Phi < \Phi_0 \tag{3}$$

and that in the region downstream of the acceleration grid is given by

$$n_e = n_\infty \exp(\Phi - \Phi_\infty)/T_{e\infty}, \qquad \Phi < \Phi_\infty \tag{4}$$

$$\simeq n_\infty[1 + (\Phi - \Phi_\infty)/T_{e\infty}], \qquad \Phi > \Phi_\infty \tag{5}$$

where Eq. (5) is the approximation of the electron density for the situation where $\Phi - \Phi_\infty$ becomes slightly positive.

In ion beamlet simulations microparticles representing propellant ions are injected into the simulation domain from the upstream boundary at every time step. The upstream density and injection velocity are input variables. How much ion current can be extracted by the optics is a function of the upstream plasma condition. In charge-exchange ion simulations microparticles representing charge-exchange ions are produced in the simulation domain at every time step according to

$$\frac{\mathrm{d}n_{\mathrm{cex}}(\boldsymbol{x})}{\mathrm{d}t} = n_b n_n v_b \sigma_{\mathrm{cex}} \tag{6}$$

where beam ion density n_b and velocity v_b are determined by the ion beamlet code and the neutral density n_n is determined by the neutral particle code. The charge-exchange ion collision cross section σ_{cex} is based on data presented in Ref. 13. The charge-exchange ions are assumed to initially follow a Maxwellian velocity distribution with a temperature corresponding to that of the unionized neutral

propellant. As the neutral temperature is only about 500 K or 0.04 eV, the initial charge-exchange ion velocity distribution has no effect on charge-exchange ion backflow.

To solve the nonlinear Poisson's equation (1) in a three-dimensional space, we have employed a dynamic alternating-direction-implicit (DADI) method[14,15] with a defect correction using the Douglass–Gunn operator splitting.[16] This DADI method was chosen over other algorithms for its increased stability properties over fully explicit methods and its relatively simple tridiagonal system of equations produced by the partially implicit nature of the method. This DADI field solver is described in Ref. 17.

The Neumann boundary condition for Φ is applied on the four side boundaries representing symmetric surfaces and the downstream boundary, while Φ is specified at the upstream boundary and the optics walls. As stated earlier, we adopt a method of subgrid-scale placement of boundaries to define the location of optics walls. For instance, consider the edge of object surface is located between grid points i and $i+1$, where grid point i is outside the conductor and grid point $i+1$ is inside the conductor. The distance between the conductor surface and grid point i is δ. We use a linear interpolation to relate the potential at the edge to that on the neighboring grid points

$$\Phi_{\text{edge}} = (1-\delta)\Phi_i + \delta\Phi_{i+1} \tag{7}$$

Note that Φ_{edge} is the known surface potential of the conductor, and Φ_{i+1} is a free parameter because it is inside the conductor. By substituting Φ_{i+1} in the finite difference form of Poisson's equation with the preceding interpolation relation: $\Phi_{i+1} = [\Phi_{\text{edge}} - (1-\delta)\Phi_i]/\delta$, we obtain the finite difference equation at the optics wall boundary. This method extends easily to three dimensions. The linear interpolation is done independently in each direction for which there is a conducting object boundary.

To properly simulate ion beam extraction from the discharge plasma, one needs to accurately resolve the sheath upstream of the screen grid. Thus, the grid resolution needs to be comparable to the Debye length of the upstream discharge plasma, and the upstream boundary needs to be placed far enough from the screen grid. To properly simulate grid erosion caused by impingement by charge-exchange ions, one needs to account for all charge-exchange ions generated downstream of the accel grid that will backflow. Thus, the downstream boundary needs to be placed far enough from the accel grid so that it is beyond the beamlet neutralization location where charge-exchange ion backflow starts.

III. Simulation Results

This three-dimensional model is used to study ion-optics plasma flow and grid erosion for the NSTAR ion thruster. Nominal NSTAR geometric dimensions at beginning-of-life and operating conditions are listed in Table 1 and are used in simulations presented here. At the end of LDT, the accel hole diameter would change from $d_a = 1.14$ to 1.36 mm as a result of erosion on the wall inside the aperture. There is little change in other geometric parameters.

The beamlet current, an important parameter used in ion-optics study, varies with the discharge plasma condition upstream of the screen grid. The simulation uses the following upstream plasma condition: discharge plasma density $n_0 = 2 \times 10^{11}$ cm^{-3}, electron temperature $T_{e0} = 5$ eV, and upstream plasma potential $\Phi_0 = 1100$ V. The downstream plasma potential is $\Phi_\infty = 0$V. The downstream electron temperature is $T_{e\infty} = 1.5$ eV, based on plume measurement.[18] We find that moderate changes in the values of T_{e0} and $T_{e\infty}$ used have little effect on grid-erosion results.

The simulation domain is shown in Fig. 2, which includes two quarter-size apertures. The beam direction is along the z direction. The hole centers are located at $(x, y) = (0, 0)$ and $(x, y) = (1.1\text{ mm}, 1.9\text{ mm})$. We take the grid resolution to be $\mathrm{d}x = \mathrm{d}z = \lambda_{D0}$ and $\mathrm{d}y/\mathrm{d}x = \tan 60$ deg. For the upstream condition considered here, $\lambda_{D0} \simeq 3.7 \times 10^{-3}$ cm.

A series of test runs on grid resolution and simulation domain size is performed to ensure that the simulation results do not depend on the numerical parameters used. In particular, we performed a series of runs where the distances between the upstream/downstream boundaries and the grid is successively increased to search for the proper simulation domain size. The final domain size is determined by examining the potential gradient and local charge-exchange ion backflow rate near the boundary. The number of cells used in the final simulation domain is $30 \times 30 \times 400$. The final simulation domain size is $0 \le \hat{x} \le 30$, $0 \le \hat{y} \le 51.96$, and $0 \le \hat{z} \le 400$, where $\hat{x}$, $\hat{y}$, and $\hat{z}$ are normalized by λ_{D0}. The upstream face of the screen grid is located at $\hat{z} = 30$, and the downstream face of the accel grid at $\hat{z} = 69.67$. Hence, the upstream boundary is located at $30\lambda_{D0}$ from the screen grid and the downstream boundary at $330\lambda_{D0}$ from the accel grid. We find that this simulation domain is sufficiently large, and the downstream location where charge-exchange ion backflow starts is explicitly included inside the domain. The number of macroparticles used in beamlet simulation is about 1.8 million, and that used in charge-exchange ion simulation is about 9 million.

Figure 3 shows beam ion velocity direction vectors (normalized by velocity magnitude). The optics extracts ions from the upstream discharge plasma and form beamlets. For the parameters listed in Table 1 with $n_0 = 2 \times 10^{11}$ cm^{-3} and $T_{e0} = 5$ eV, we find that the current extracted is $I_b \simeq 0.184$ mA/beamlet. The screen grid transparency is about 73%, and the accel grid transparency is 100%. Figure 4 shows the three-dimensional structure of potential

Table 1 Nominal geometric and operating parameters for the NSTAR ion engine

Parameters	Value
Screen hole diameter d_s	1.91 mm
Screen grid thickness t_s	0.38 mm
Accel hole diameter d_a	1.14 mm
Accel grid thickness t_a	0.51 mm
Screen to accel grid gap g	0.58 mm
Center-to-center hole spacing l	2.21 mm
Total accelerating voltage	1100 V
Screen grid voltage	1074 V
Accel grid voltage	−180 V
Propellant utilization efficiency	90%

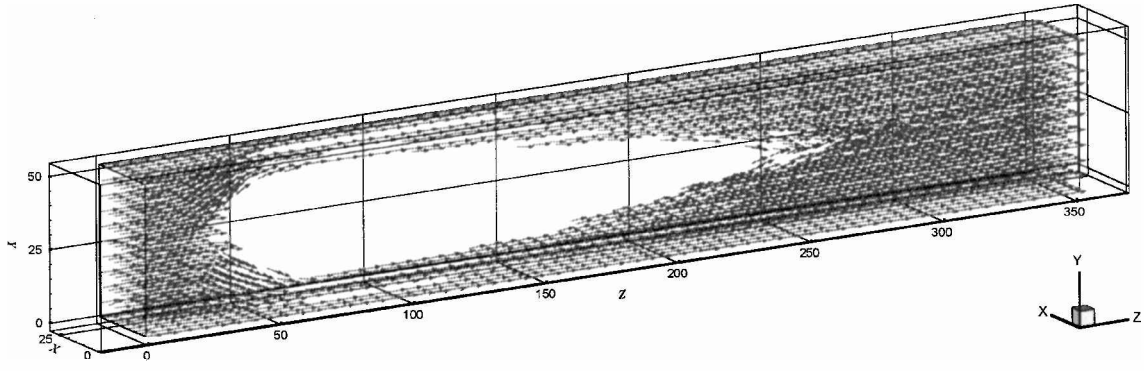

Fig. 3 Beam ion velocity direction vectors.

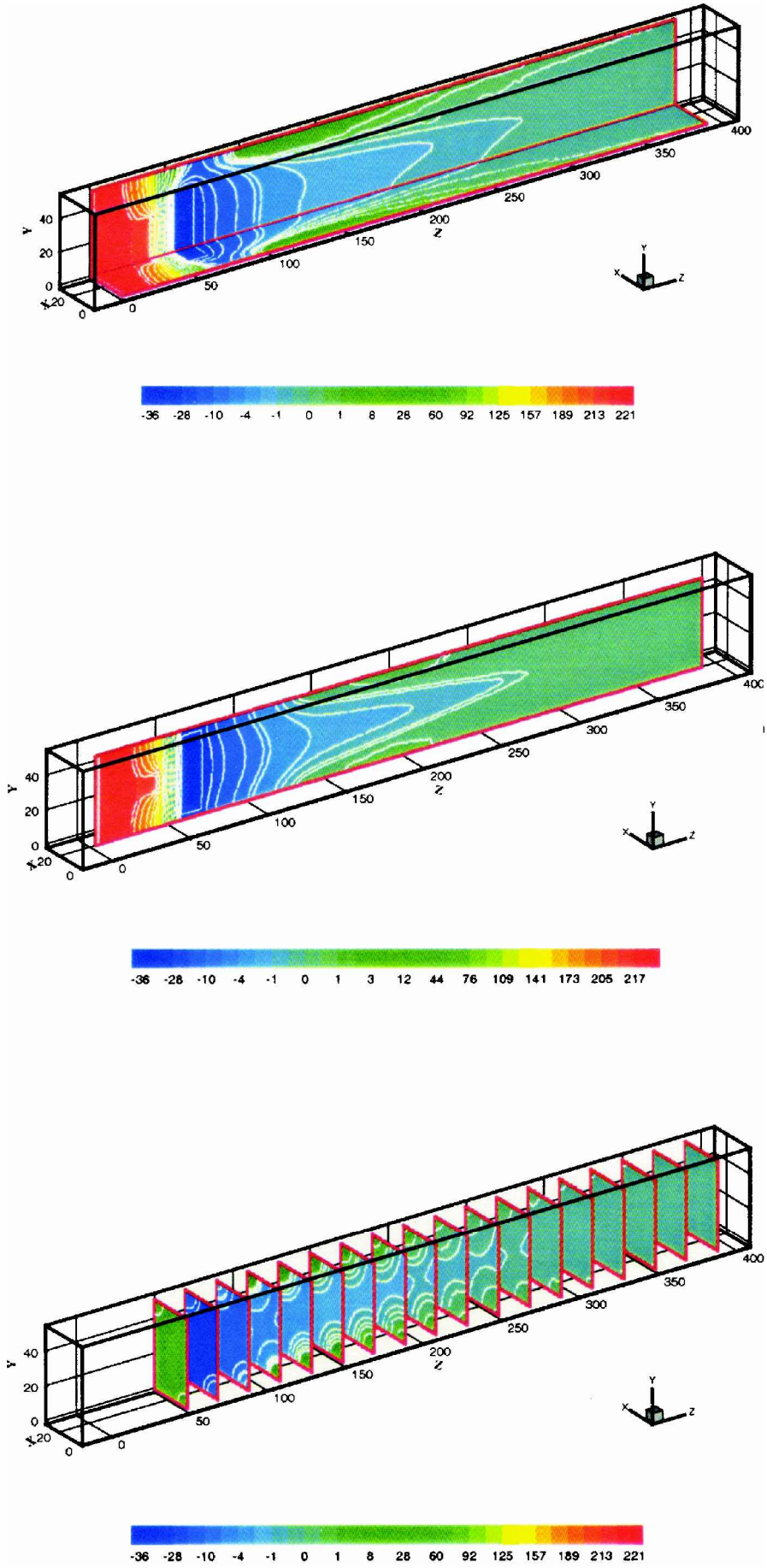

Fig. 4 Electric potential contours (contour values normalized by 5 V): upper panel, contours on the side boundary surfaces at $y = 0$ and $x = 1.1$ mm; middle panel, contours on a z–y surface cutting through the middle of the simulation domain; and bottom panel, contours on several x–y cutting planes.

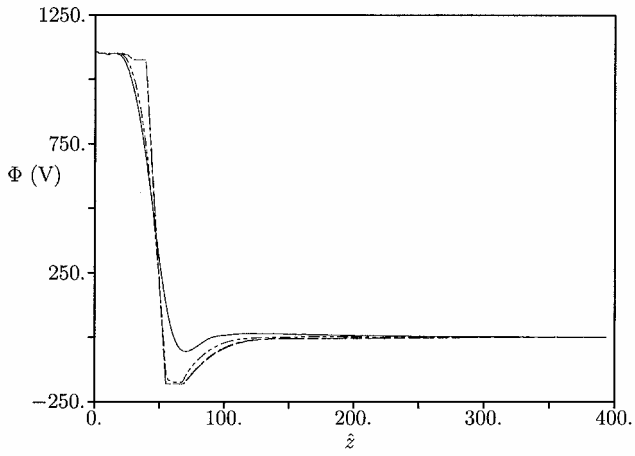

Fig. 5 Potential profiles along the beam direction: ——, z axis through $(x, y) = (0, 0)$ (beamlet center); – – –, z axis through $(x, y) = (0, 1.27$ mm); . . . . , z axis through $(x, y) = (0.55$ mm, 0.96 mm) (hole-to-hole center); and -.-, z axis through $(x, y) = (0.55$ mm, 0 mm).

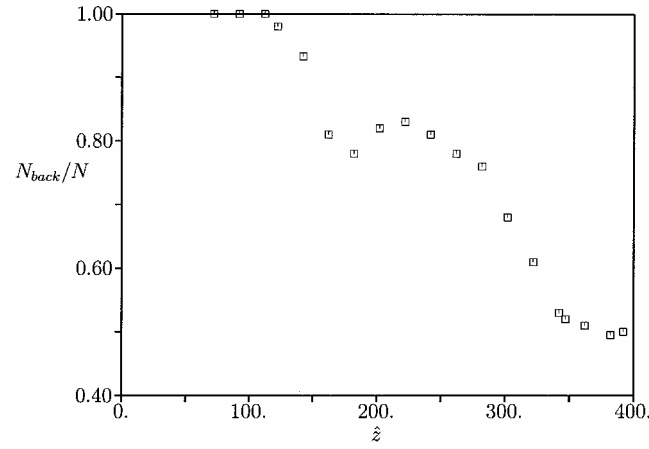

Fig. 6 Local charge-exchange ion backflow rate $N_{\text{back}}(z)/N(z)$.

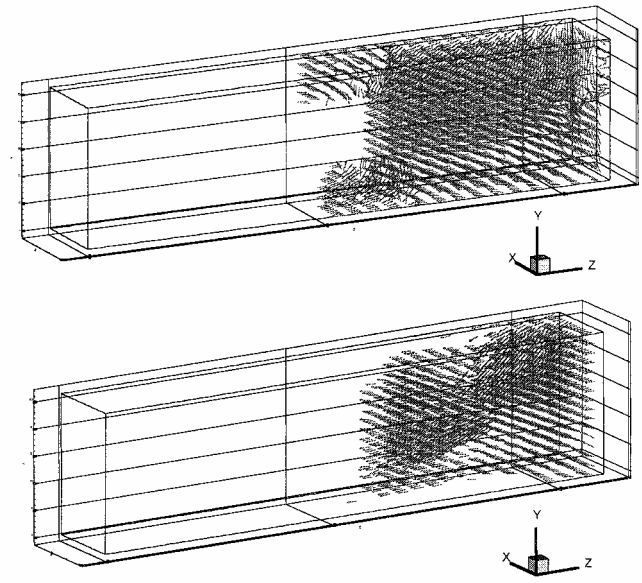

Fig. 7 Charge-exchange ion velocity direction vectors in the downstream region of the accel grid; upper panel, charge-exchange ions originated in the near-grid zone; and bottom panel, charge-exchange ions originated in the far-downstream zone.

contours. The upper panel shows potential contours on the side boundary surfaces at $y = 0$ and $x = 1.1$ mm. The middle panel shows contours on a $z - y$ surface cutting through the middle of the simulation domain. The bottom panel shows contours on several $x - y$ cutting planes. Effects from the grid surface potential and the space charge of the beamlet are apparent in the potential contours. Figure 5 shows potential profile along several characteristic axes in the z direction. We find that the neighboring beamlets start to overlap at about 0.75 cm downstream of the accel grid ($\hat{z} \sim 202$). Starting at about 1.1 cm downstream of the grid ($\hat{z} \sim 360$), beamlet mixing is complete, and the potential profile becomes flat, indicating that the beamlets are neutralized by the downstream plasma.

The unionized propellant flow is related to the ion beamlet through propellant utilization efficiency. For the operating condition considered here, we find that the neutral density upstream of the screen grid is $n_{n0} \simeq 1.5 \times 10^{12}$ cm^{-3}, and the neutral flow rate through the thruster is 2.67×10^{-6} kg/s. These conditions are used in the neutral particle code to calculate the neutral density distribution in the simulation domain. The results, coupled with beam ion density profile, are used to generate charge-exchange ion production rate in the simulation domain.

To understand the behavior of charge-exchange ions generated in the downstream region and identify the location where charge-exchange ion backflow starts, we first examine the local charge-exchange ion backflow rate. We divide the downstream region into slices along the z direction and track the motion of the charge-exchange ions generated within each slice. Let $N(z)$ denote the total number of particles generated in a slice located at z within a time step dt. Among these particles $N_{\text{back}}(z)$ number of particles would eventually backflow toward the accel grid. Hence, we define the local charge-exchange ion backflow rate for each slice as the ratio of $N_{\text{back}}(z)/N(z)$. Obviously, one would expect $N_{\text{back}}(z)/N(z) \simeq 0.5$ if there is no external electric field to preferentially influence the motion of charge-exchange ions.

Figure 6 shows the $N_{\text{back}}(z)/N(z)$ profile. We find $N_{\text{back}}(z)/N(z) \simeq 0.5$ in the region beyond 1.1 cm downstream of the accel grid ($\hat{z} > 360$). This indicates that in this region the beamlets are fully neutralized, and hence the charge-exchange ions are in thermal equilibrium. On the other hand, we find $N_{\text{back}}(z)/N(z) = 1$ in the region within a distance of about 0.15 cm downstream of the accel grid ($\hat{z} < 110$). This indicates that all charge-exchange ions born in this region will backflow because of the attraction of the accel grid potential.

A comparison of Figs. 5 and 6 suggests that one can divide the simulation domain into a near-grid zone and a far-downstream zone for the analysis of charge-exchange ion backflow. The near-grid zone is the region immediately downstream of the accel grid where there is a steep potential gradient with electric field pointing toward the accel grid. The far-downstream zone is the region beyond the near-grid zone where there is a net charge-exchange ion backflow even though the potential gradient might be very small. For the case shown here, one can define the near-grid zone as the region within about 0.15 cm ($\hat{z} < 110$) downstream of the accel grid and the far-downstream zone as the region between 0.15 to 1.1 cm ($110 < \hat{z} < 360$) downstream of the accel grid. Charge-exchange ion backflow starts at about 1.1 cm ($\hat{z} \sim 360$) downstream of the accel grid. As one moves from $\hat{z} \sim 360$ toward $\hat{z} \sim 200$, the influence of the accel grid potential on charge-exchange ions increases, and so does $N_{\text{back}}(z)/N(z)$, which exhibits a dip in $150 < \hat{z} < 200$. This nonmonotonic behavior is caused by a positive potential bump inside the beamlet caused by ion focusing.

Both the flow characteristics and impingement characteristics are very different for those ions born in the near-grid zone and those in the far-downstream zone. Figure 7 shows charge-exchange ion velocity direction vector in the downstream region of the accel grid. We plot separately for those charge-exchange ions originated in the near-grid zone and those originated in the far-downstream zone. We find that 62% of the charge-exchange ions born in the near-grid zone is collected by the downstream face, and the rest is collected by the wall inside the aperture. On the other hand, 100% of the charge-exchange ions originated in the far-downstream zone hit the

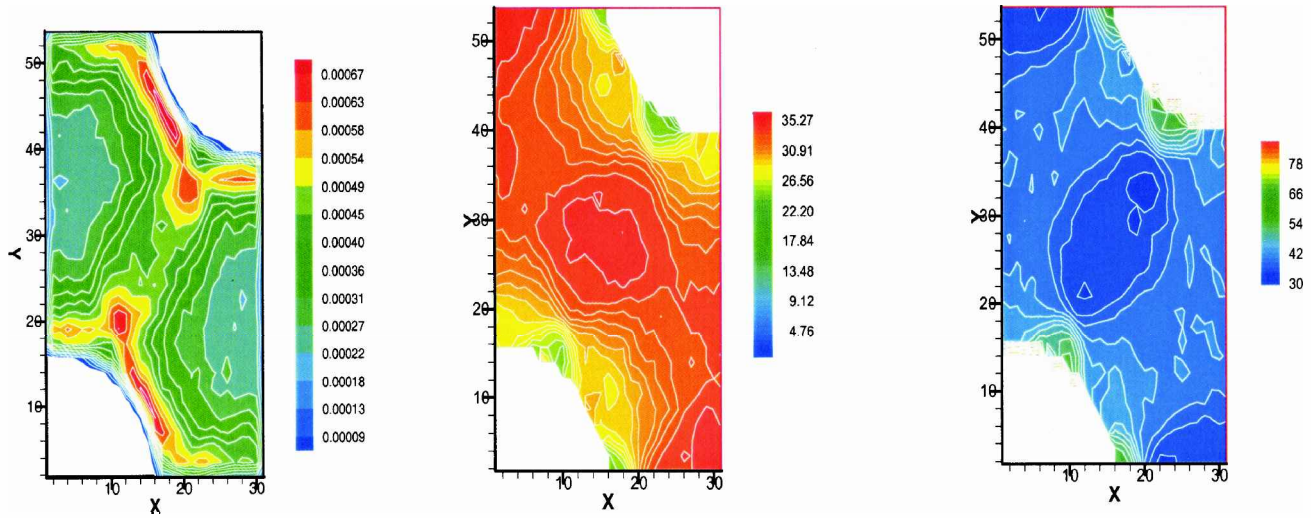

Fig. 8 Impingement on accel grid downstream surface by the charge-exchange ions originated in the near-grid zone; left, impingement current density distribution; middle, impingement energy distribution; and right, incident angle distribution.

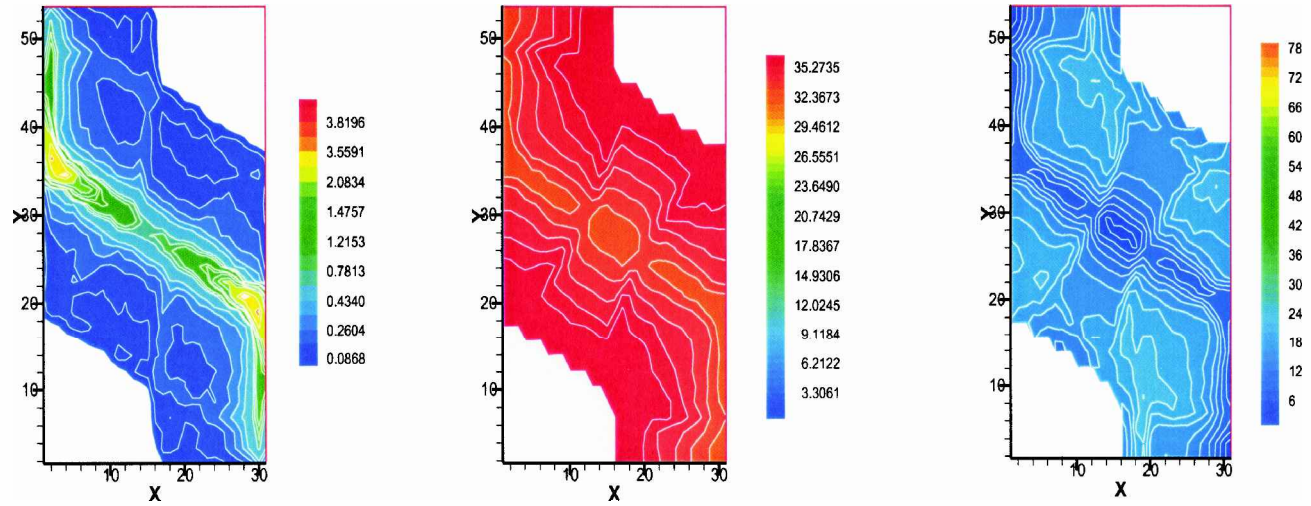

Fig. 9 Impingement on accel grid downstream surface by the charge-exchange ions originated in the far-downstream zone: left, impingement current density; middle, impingement energy; and right, incident angle.

downstream face of the accel grid. The charge-exchange ions originated in the near-grid zone contribute to less than 12% of the total number of ions impinged upon the accel grid surface in our simulation domain. Hence, the impingement current is dominated by charge-exchange ions born in the far-downstream zone. One can significantly underpredict the accel grid current if one fails to include the far-downstream zone in the simulation domain.

Figures 8 and 9 show contours of the impingement ion current density, ion energy distribution, and incident angle distribution on the downstream surface of the accel grid. Again, we plot separately for those charge-exchange ions originated in the near-grid zone and those originated in the far-downstream zone. The results shown in Figs. 8 and 9 are used to calculate grid erosion.

IV. Grid Erosion: Comparison with Measurements

In this section we compare the measured erosion pattern and erosion depth on the downstream face of the accel grid with that calculated based on simulation results. We calculate the depth erosion rate R from

$$R = \frac{JY(E,\theta)M_{\mathrm{Mo}}}{e\rho_{\mathrm{Mo}}} \tag{8}$$

where J is impingement current density, Y the sputter yield, E incident energy, θ incident angle, M_{Mo} the mass of Mo, and $\rho_{\mathrm{Mo}} \simeq 10220\,\mathrm{kg/m^3}$ the density of Mo. The sputter yield, a function of incident particle energy and angle, is obtained from curve fitting to measured low-energy sputter yield data.[19] The distributions of impingement current density incident energy and incident angle on grid surface are obtained from simulation and are shown in Figs. 8 and 9.

During the long-duration test of the NSTAR ion thruster, both laser profilometer measurements and posttest destructive exams were performed to measure accel grid erosion.[9] For comparison, we select measurement for an aperture at a location where the measured beamlet current is approximately the same as that in the simulation. Comparing the value of the extracted beam current in the simulation with the measured ion beamlet profile over the NSTAR grid,[9] we find that the simulation case presented here corresponds to an aperture at about 5.8-cm radius from thruster center.

Figure 10 compares the erosion pattern on the downstream surface of the accel grid. The left panel is a photograph of erosion pattern after 8200 h of operation, the middle panel shows erosion pattern calculated from simulation results for the same operating conditions, and the right panel overlays simulation results on experimental data.

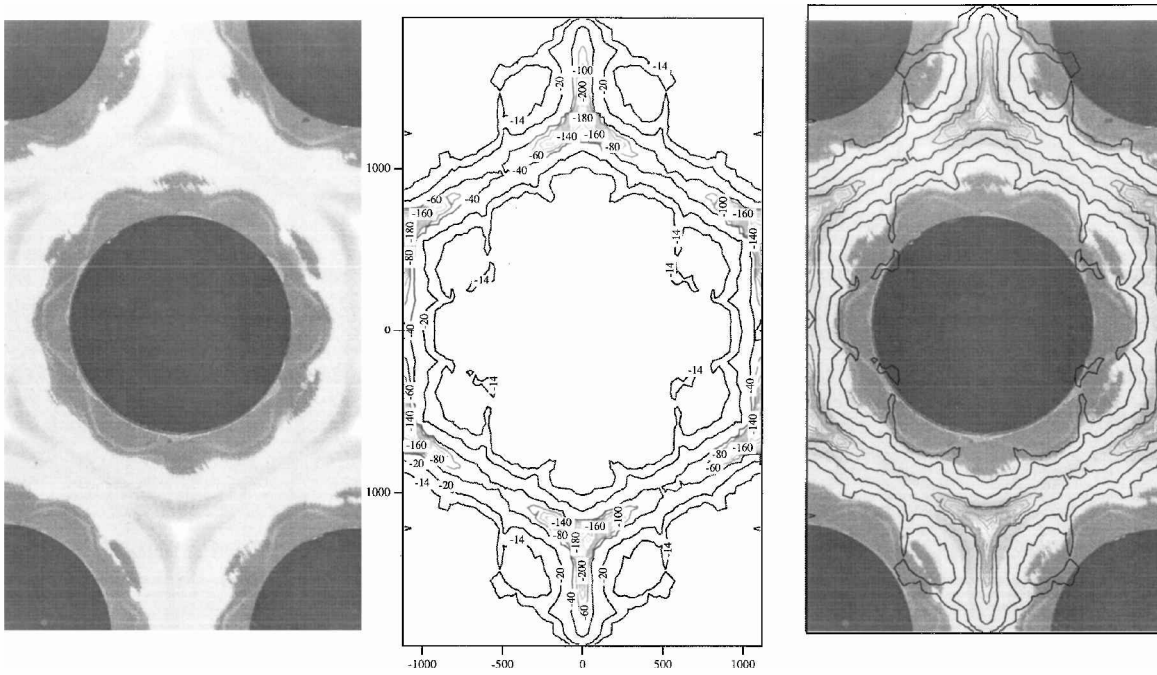

Fig. 10 Comparison of simulation results with experimental data. Grid-erosion pattern on accel grid downstream surface: left, photograph of erosion and deposition pattern after 8200 h of operation; middle, simulation results for the same operating conditions; and right, direct comparison of the erosion pattern.

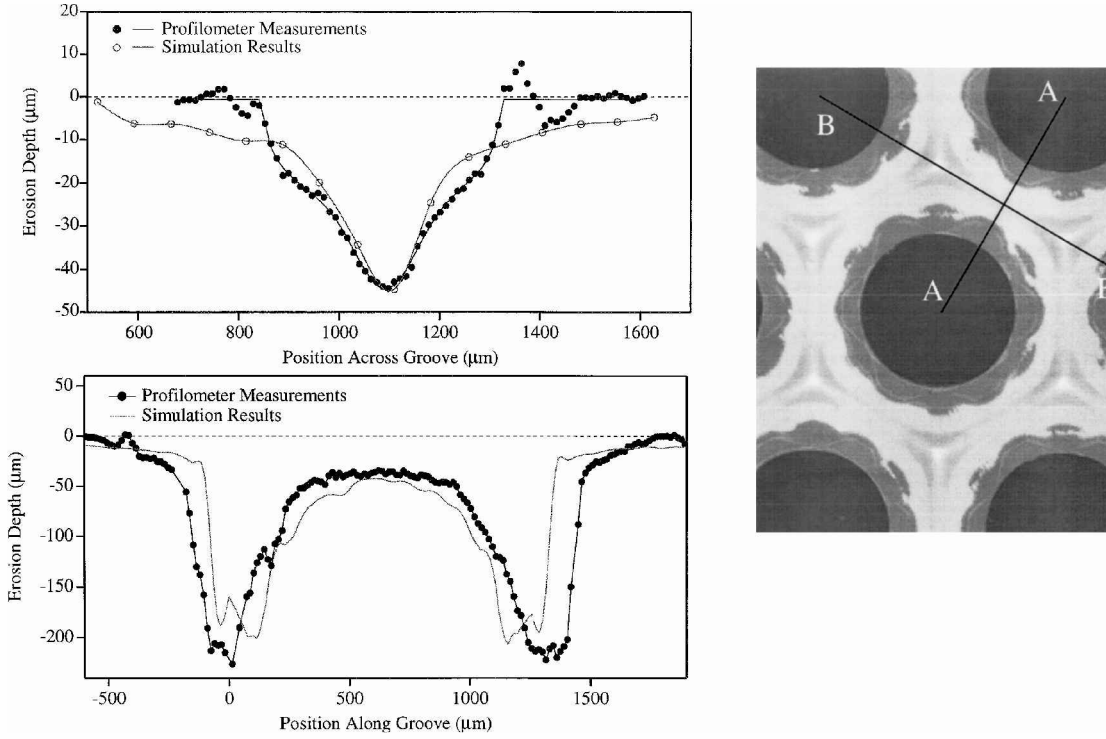

Fig. 11 Comparison of simulation results with experimental data. Grid-erosion depth on accel grid downstream surface: upper left, erosion depth profile across the groove (A-A); bottom left, erosion depth profile along the groove (B-B); and right, locations of the A-A and B-B profile on grid surface.

The figure shows that the simulation picks up all of the detailed features shown in the measured erosion pattern.

Figure 11 compares erosion depth along and across the groove. The maximum eroded depth from simulation is about 208 μ, whereas the pit depth from the long duration test is 220–230 μ. The simulation also shows an excellent agreement with the measurement in the groove pattern. The net erosion on the plateau around the pits and grooves from simulation appears to disagree with the profilometer data. The reason that less erosion is observed in these locations is because carbon deposits protected the grid in these locations during the LDT. Figures 10 and 11 show that the simulation not only accurately predicts the erosion pattern but also gives excellent quantitative agreement with erosion measurements.

V. Conclusions

In summary, a fully three-dimensional particle simulation model for ion optics has been developed. Out of consideration for computational efficiency for large-scale simulations, this code is built upon

standard orthogonal grids and a finite difference based formulation. The three-dimensional optics aperture geometry is handled by a method of subgrid-scale placement of boundaries, which explicitly includes the location of the optics wall in relation to the grid in the finite difference form of Poisson's equation. Multiple apertures can be included explicitly in the simulation domain. Ion beam extraction from the discharge plasma is calculated self-consistently. The location where beamlets are neutralized and charge-exchange ions start to backflow is determined from the simulation. We find that the accel grid current and the erosion on the downstream face of the accel grid are primarily caused by those charge-exchange ions originated in the far downstream region. This three-dimensional particle simulation model is applied to study optics plasma flow and grid erosion for the NSTAR ion thruster. Grid erosion predicted by simulation is compared against erosion measurements taken during the long-duration test of the NSTAR ion thruster. The simulation not only resolves accurately all of the features in the measured erosion pattern but also gives excellent quantitative agreement with measured erosion depth.

Acknowledgments

We would like to acknowledge the assistance from R. Kafafy in producing three-dimensional plots of the simulation results and M. Young in developing the three-dimensional dynamic alternating-direction-implicit field solver. This work is carried out through support from the Jet Propulsion Laboratory (JPL), California Institute of Technology, under a contract with NASA. Simulations are performed on the Cray SV-1 supercomputer at JPL. Access to the JPL supercomputer was provided by funding from NASA Offices of Mission to Planet Earth, Aeronautics, and Space Science.

References

[1]Peng, X., Ruyten, W., Friedly, V., Keefer, D., and Zhang, Q., "Particle Simulation of Ion Optics and Grid Erosion for Two-Grid and Three-Grid Systems," *Review of Scientific Instruments*, Vol. 65, No. 5, 1994, pp. 1770–1774.

[2]Arakawa, Y., and Nakano, M., "An Efficient Three-Dimensional Optics Code for Ion Thruster Research," AIAA Paper 96-3198, July 1996.

[3]Boyd, I., VanGilder, D., and Liu, X., "Monte Carlo Simulation of Neutral Xenon Flows in Electric Propulsion Devices," *Journal of Propulsion and Power*, Vol. 14, No. 6, 1998, pp. 1009–1015.

[4]Nakano, M., and Arakawa, Y., "Ion Thruster Lifetime Estimation and Modeling Using Computer Simulation," *26th International Electric Propulsion Conference*, IEPC 99-145, Oct. 1999.

[5]Tartz, M., et al., "Validation of a Grid-Erosion Simulation by Short-Time Erosion Measurements," *26th International Electric Propulsion Conference*, IEPC 99-147, Oct. 1999.

[6]Okawa, Y., and Takegahara, H., "Particle Simulation on Ion Beam Extraction Phenomena in an Ion Thruster," *26th International Electric Propulsion Conference*, IEPC 99-146, Oct. 1999.

[7]Muravlev, Y., and Shagayda, A., "Numerical Modeling of Extraction Systems in Ion Thrusters," *26th International Electric Propulsion Conference*, IEPC 99-162, Oct. 1999.

[8]Nakayama, Y., and Wilbur, P., "Numerical Simulation of Ion Beam Optics for Many-Grid Systems," AIAA Paper 2001-3782, July 2001.

[9]Polk, J., Anderson, J., Brophy, J., Rawlin, V., Patterson, M., Sovey, J., and Hamley, J., "An Overview of the Results from an 8200 Hour Wear Test of the NSTAR Ion Thruster," AIAA Paper 99-2446, July 1999.

[10]Westermann, T., "Localization Schemes in 2D Boundary-Fitted Grids," *Journal of Computational Physics*, Vol. 101, No. 2, 1992, pp. 307–313.

[11]Wang, J., Kondrashov, D., Liewer, P., and Karmesin, S., "Three-Dimensional Deformable Grid Electromagnetic Particle-in-Cell for Parallel Computers," *Journal of Plasma Physics*, Vol. 61, No. 3, 1999, pp. 367–389.

[12]Grote, D., "Three-Dimensional Simulations of Space-Charge Dominated Heavy Ion Beams with Applications to Inertial Fusion Energy," Ph.D. Dissertation, Univ. of California, Davis, June 1994.

[13]Pullins, S., Chiu, Y., Levandier, D., and Dressler, R., "Ion Dynamics in Hall Effect and Ion Thrusters: $Xe^{+} + Xe$ Symmetric Charge Transfer," AIAA Paper 2000-0603, Jan. 2000.

[14]Doss, S., and Miller, K., "Dynamic ADI Methods for Elliptic Equations," *SIAM Journal of Numerical Analysis*, Vol. 16, No. 5, 1979, pp. 837–855.

[15]Hewett, D., Larson, W., and Doss, S., "Solution of Simultaneous Partial Differential Equations Using Dynamic ADI," *Journal of Computational Physics*, Vol. 101, No. 1, 1992, pp. 11–24.

[16]Douglass, J., and Gunn, J., "A General Formulation of Alternating Direction Methods," *Numerische Mathematik*, Vol. 6, No. 2, 1964, pp. 428–453.

[17]Wang, J., Brinza, D., and Young, M., "3-D Particle Simulation Modeling of Ion Propulsion Plasma Environment for Deep Space 1," *Journal of Spacecraft and Rockets*, Vol. 38, No. 3, 2001, pp. 433–440.

[18]Wang, J., Brinza, D., Young, D., Nordholt, J., Polk, J., Henry, M., Goldstein, R., Hanley, J., Lawrence, D., and Shappirio, M., "Deep Space One Investigations of Ion Propulsion Plasma Environment," *Journal of Spacecraft and Rockets*, Vol. 37, No. 5, 2000, p. 545.

[19]Rosenberg, D., and Wehner, G. K., "Sputtering Yields for Low Energy He+, Kr+, and Xe+ Ion Bombardment," *Journal of Applied Physics*, Vol. 33, No. 5, 1962, pp. 1842–1845.